Modified crystal structure and improved photocatalytic activity of MIL-53 via inorganic acid modulator

Danni Jiang[a,b,1], Yuan Zhu[a,b,1], Ming Chen[a,b,1], Binbin Huang[a,b,1], Guangming Zeng[a,b,*], Danlian Huang[a,b,*], Biao Song[a,b], Lei Qin[a,b], Han Wang[a,b], Wei Wei[c,b]

[a] College of Environmental Science and Engineering, Hunan University, Changsha, 410082, PR China
[b] Key Laboratory of Environmental Biology and Pollution Control, Hunan University, Ministry of Education, Changsha, 410082, PR China
[c] Longping Branch Graduate School, Hunan University, Changsha, 410082, Hunan Province, PR China

ABSTRACT

Metal-organic frameworks (MOFs) as photocatalysts have attracted considerable attention due to their potential for environment remediation, of which MIL-53 is a representative member of MOFs. However, the photocatalytic performance was affected by the recombination of photo-generated electron-hole pairs. On the one hand, acid-modulated MOFs have received much attention, however, more attention have been paid to the adsorption capacity and there is still a big gap in the application of photocatalysis. This work focused on the effect of HCl modulator on crystal structure and photocatalytic activity. In the morphology aspect, the presence of smaller crystals and layer structure and mesoporous distribution was due to the regulatory effect of HCl, and it had a double function: slowing down the hydrolysis of $FeCl_3 \cdot 6H_2O$ as well as conteracting the deprotonation of the dissovled carboxylic acids. Notablely, as demonstrated by XRD, the change of crystal form from MIL-53 to MIL-88 was attributed to the presence of 40 µL. Increased specific surface area could provide more adsorptive and catalytic sites. Compared with the MIL-53, the photocatalytic activity of acid-regulated MIL-53 increased by 1.5 times. Meanwhile, the quantitative relationship between the photocatalytic activity and the content of HCl was revealed. Finally, $\cdot O_2^-$ and $\cdot OH$ as the main active free radicals in photocatalytic degradation process were confirmed by the EPR analysis. This work provides a basis for the application of modulated MOFs by acid modulator in photocatalysis.

1. Introduction

Metal-organic frameworks (MOFs) as a class of porous crystalline materials, based on the coordination bonds between metal clusters have attracted considerable attention over the past few decades [1–3]. The abundant pore size and adjustable structure make the MOFs widely used in many fields [4–7], including gas storage and separation, catalysis, drug transport, proton conductors, *etc*. In particular, some MOFs with semiconductor properties can be used for the photocatalytic degradation of organic pollutants [8–11].

Defects, refer to irregular arrangement of crystal atoms, and they are widely exist in MOFs, which aroused great interest among the researchers. Structural disorder and heterogeneity within MOFs breaks the periodic arrangement of atoms and greatly influences the pore/aperture sizes as well as the surface properties of the resulting materials, which subsequently modifies their performance [12–14]. The

targeted incorporation of defects into MOFs, *i.e.*, the synthetic control of the concentration and chemical nature of defect, remains challenging until today [15]. The methods of prepared defects reported divided into two categories, (i) the "de novo" synthesis, including modulation approach, mixed linker approach, fast crystal growth. (ii) the post synthetic treating synthesis, including mechanical treatment, acid/base treatment, harsh activation procedure [16]. To date, the modulator strategy, as the most common one, refers to the addition of large amounts modulator in addition to the linker molecules into the precursor solution during the MOF synthesis. It is generally accepted that small amounts of modulator slow down the speed of crystallization by impacting the equilibrium reaction and in turn the formation of defects. It is worth noting that the existing modulator are applied to MOFs with carboxylic acid as linker, typically UiO-66 was the mode system for many works [17–19].

In recent years, the study on the effect of crystal morphology and

properties by the modulators has been updated gradually. Compare to UiO-66, the TFA (Trifluoroacetic acid)-modulated UiO-66 sample was found to be significantly more active. Modulator-dependent defect engineering can also be used as a tool for pore design in order to facilitate diffusion and to incorporate different catalytically active species. The particle size of the $Cu_3(BTC)_2$ (HKUST-1) could be tuned from 300 nm to 2.4 μm by varying the amount of CA added [20]. The intrinsic microporous structure of HKUST-1 is maintained while the larger pores' size distributed in the range of 30 to 100 nm. After encapsulation, a superior catalytic activity with a high conversion rate is achieved. TMA (Trimesic acid) as a modulator, could optimize the HKUST-1 with nanosize and the modulated one exhibited the increased adsorption for CO_2 with the adsorption capacity of 2.5 mmol /g [21]. In the work of Bagherzadeh, *et al.*, acetic acid and formic acid were chosen as monoligand modulated agents for MIL-88 A. At low modulator content, the primary diamondlike characteristic morphology of the particles was preserved. While acetic acid mildly altered the morphology of the MOF and narrowed its particle-size distribution, on the other hand, formic acid is more potent than acetic acid, which drastically changed the morphology of the MOF particles to those resembling dendrites [22]. Atzori et al. recently reported on the specific influence of benzoic acid modulator toward the formation of missing cluster defects. Specially, the quantitative relationship between defects and modulator was confirmed from the combination of PXRD, dissolution/^{1}H NMR spectroscopy and N_2 sorption measurements [23]. Cai and Jiang reported on the hierarchical UiO-66 containing mesoporous using acetic/octanic/dodecanic acid as modulators [24]. The pore diameter in the obtained defective UiO-66 systems was systematically turned *via* altering the length and concentration of the modulator, resulting in smaller or bigger mesopores within the microporous UiO-66. The defect-induced formation of mesopores allows for the incorporation of larger catalytically active species like polyxometallates, which then can be used in the catalytic methanolysis of styrene oxide. Except the novo synthesis, generally, defects can be formed by post-synthetic treatment (such as acid/based treatment and solvent exchange).

However, the current studies focused on the adsorption and catalytic properties of modulated MOFs by acid modulator, and there is still a gap in the effect of modulator on the photocatalytic properties. In this work, Fe(III)-based MOFs with photocatalytic activity, as a member of the MIL family, were selected as the research object for the photocatalytic degradation of tetracycline with persistance and potential harm to the environment. MIL-53, as a typical porous Fe-MOF, possesses a strong Fe-O clusters as light absorbing component responsible for photocatalytic activity; however, the photocatalytic performance of which was affected by the recombination of photo-generated electron-hole pairs. There was much space retained to improve the photocatalytic activity, mainly, additional electron acceptors and heterojunction structures, and both are conductive to charge and holes separation. The hydrogen peroxide (H_2O_2), persulfate (PS) and peroxymonosulfate (PMS) as electron acceptors accelerated the photocatalytic process by promoting the separation of photogenerated electrons and holes [21–25]. In addition, the heterojunction based on MIL-53, including the MIL-53/AgI [26–28], MIL-53/Ag_3PO_4 [28,29], MIL-53/SnS [30] and MIL-53/g-C_3N_4 [31–33] are effective in photocatalytic degradation of organic pollutants. However, the increased photocatalytic activity of single crystal MIL-53 by acid modulator has not been reported until now. This work focused on the effect of acid modulator on the crystal morphology, size and photoelectric properties, the emphasis on the photocatalytic activity. In particular, the quantitative relation between the content of HCl modulator and the phtocatalytic activity has been revealed. This work provides a basis for the application of modulated MOFs by acid modulator in photocatalysis.

2. Materials and methods

2.1. Materials

1,4-Benzenedicarboxylic acid (H_2BDC, 99%), *N,N*-dimethyformadie (DMF, 99%) were purchased from Sinopharm Chemical Reagent Co., Ltd (Shanghai, China). Iron (III) chloride hexahydrate ($FeCl_3 \cdot 6H_2O$, 99%) and hydrochloric acid (HCl) were supported by Macklin chemical Reagent Co., Ltd (Shanghai, China). All the reagents were obtained from commercial channels and were of analytic grade without further purification.

2.2. Synthesis of single crystal MIL-53

MIL-53 (Fe) was prepared by a facile solvothermal method [34]. A mixture of $FeCl_3 \cdot 6H_2O$, H_2BDC and DMF with a molar ratio of 1: 1: 280 was stirred until the formation of bright yellow clear liquid. Then, the reaction mixture was heated at 170 °C for 24 h in a Teflon-lined stainless steel autoclave. The sample was vacuum filtered and cleaned by DMF and methanol three times. The obtained orange-yellow precipitate was dried under vacuum at 70 °C.

2.3. Synthesis of defective MIL-53

Defective MIL-53 (Fe) was prepared by the acid modulation method on the basis of as-obtained MIL-53. Different amounts of HCl (10 μL-40 μL) (1 M/L) was added into the mixture of $FeCl_3 \cdot 6H_2O$, H_2BDC and DMF until a nice mixture. Then, the reaction mixture was heated at 170 °C for 24 h in a Teflon-lined stainless steel autoclave. The filtration, cleaning and drying processes are similar to MIL-53. 10 μL, 20 μL, 30 μL, 40 μL, 50 μL, 100 μL HCl modulated samples were denoted as D-1, D-2, D-3 and D-4, D-5 and D-10.

2.4. Characterization

The crystals structures of the samples were determined by X-ray diffraction (XRD, XRD-6100, Shimadzu) with Cu Ka radiation, operating at 2θ range from 10° to 80°. Fourier transformation infrared (FTIR) spectra on KBr pellets of the samples were analyzed on a Nicolet FTIR 5700 spectrometer at a resolution of 4 cm^{-1}. The Brunauer-Emmett-Teller (BET) specific surface areas and pore size distribution were measured on a surface area analyzer (Belsorp-miniII, BEL) by nitrogen adsorption-desorption. X-ray photoelectron spectroscopy (XPS) was analyzed on a spectrometer (Escalab 250Xi, Thermo) using an Al Ka X-ray source (1486.6 eV). The ultraviolet visible diffused reflectance spectra (UV–vis DRS) were collected on an UV–vis spectrophotometer (Cary 300, Varian) in the wavelength range from 300 nm to 800 nm with $BaSO_4$ as the reference. The optical band gap of MIL-53(Fe) could be calculated according to the energy dependence relation of ahv = $A(hv-E_g)^{n/2}$, where a,h,Eg, and A are absorption coefficient, Plant constant, light frequency, optical band gap and a constant, respectively and n is determined by the type of optical transition in the semiconductor (n = 1 for a direct transition). The photoluminescence (PL) spectra were obtained on a Hitachi F-4500 fluorescence spectrophotometer at an excitation wavelength of 340 nm. The photocurrent, impedance and Mott-Schottky measurements were conducted with a CHI760E electrochemical workstation. For the preparation of photoelectrodes, the photocatalysts were dispersed in polyvinyl alcohol solution to form a 2 mg/L solution and ultrasonicated for 60 min. Then, indium doped tin oxide (ITO) conductive glass was covered with 100 μL colloidal solution and dry at 60 °C. The measurements were performed in a standard three-electrode system, including working electrode (ITO), the counter electrode (Pt), and the reference electrode (saturated calomel electrode) and 0.5 M Na_2SO_4 aqueous solution as the electrolyte. The electron spin response (ESR) signals of free radical were examined on a spectrometer (JES-FA200, JEOL) under visible light

irradiation (λ > 420 nm) using 5,5-dimethyl-1-pyrroline N-oxide (DMPO) as spintrapped reagent

2.5. Photocatalytic activity tests

The photocatalytic activities of MIL-53 and defective MIL-53 were evaluated by the targeted tetracycline TC under visible light irradiation. Visible illumination was obtained by a 300 W Xe lamp (CEL-HXF300, Ceaulight) equipped with a 420 nm cutoff filter. Typically, 50 mg of the sample was dispersed into a 100 mL of 20 mg/L TC aqueous solution. Prior to irradiation, the suspensions were fiercely magnetically stirred for 60 min in the dark to reach the adsorption-desorption equilibrium. Then, TC solution can be treated under light conditions. Every 30 min, 4 mL of the reaction suspensions were taken out and filtered out the photocatalyst power, and the concentration of TC was monitored by an UV–vis spectrophotometer (UV-2700, Shimadzu) under 357 nm excitation wavelength. The removal efficiency (DE, %) was calculated by the following equation:

$$DE(\%) = (C_0 - C_t)/C_0 \times 100\%$$

Where C_0 is the initial concentration of TC, and C_t is the TC concentration at time t.

3. Result and discussion

3.1. Characterization of materials

Fig. 1a shows the XRD patterns of MIL-53, D-1, D-2, D-3 and D-4. In the XRD patterns of MIL-53, the diffraction peaks located at 9.238° (110), 9.785° (200), 16.630° (112), 18.551° (220) respectively, which were in good agreement with the simulated patterns [35,36]. Meanwhile, the crystalline nature of the products was confirmed by the sharp diffraction peak and high diffraction peak intensity [37]. In the XRD, with the increased dosage of HCl (10, 20 to 30 μL), the peak intensities of XRD was obviously reduced, interestingly, when the dosage of HCl increased to 40 μL, the new diffraction peak corresponding to MIL-88(Fe) appeared. The results showed that HCl played an important role in the transformation between different crystals forms of Fe-based MOFs. Sanil [38] reported the effect of dodecanoic acid on the crystallinity and morphology of MOF of copper 1,3,5-benzenetricarboxylate (Cu-BTC). The modulated samples show wellresolved prominent diffraction peaks characteristic of CuBTC crystals. A line-broadening and lower of main peak in the XRD patterns was observed. In the study of Zhao [39], acetic acid was used as an effective coordination modulator to modulate the size, morphology and crystal form of MIL-101 (Fe). A good yield and product quality could be reached compared to experiments without addition of acetic acid. With increased addition of acetic acid (5,10,15,20,25,30 mL), the XRD peak intensity decreased. Notably, while the patterns of A-35(mL) and A-40(mL) possessed a stronger reflection at 2 θ = 10.92°, which pointed to the rod-like by-product (MIL-53). Others, benzoic acid played an important role in the conversion between MIL-88 and MIL-101(Cr) [40]. HBC-0, HBC-1 and HBC-3 samples, when using 0,1,3 equivalents of the benzoic acid additive, exhibit particles with an octahedral morphology, characteristic of MIL-101(Cr). Interestingly, the increase of benzoic acid concentration to nearly double or more, which corresponds to the use of 5, 8 or 10 equivalents,caused the formation of lesser amounts or no MIL-101(Cr). Indeed, for HBC-8, the content of nano-MIL-101(Cr) decreases further and the rod-like MIL-88B (Cr) became dominant,while for HBC-10 only the micrometer-sized rod-like crystals of MIL-88B (Cr) were observed. Thereby an interesting effect of a relatively sharp change of crystallization outcome depending on the concentration of the benzoic acid was observed, with a higher concentration favoring the MIL-88(Cr) form. During the crystal formation, HCl had a double function: it slowed down the hydrolysis of $FeCl_3.6H_2O$ and counteracted the

deprotonation of the dissolved carboxylic acids. The proper acid-base environment of the reaction system governed deprotonation of the organic linker and the crystal nucleation process [41]. The other is that the HCl as a capping agent inhibited crystallites from growing.

The effect of HCl modulator on the functional group of MIL-53 was reflected in the infrared spectrum (FTIR). Since defects in the MOF lattice may play a major role in the electronic and optical properties of the material [42], the defects and their densities were investigated by FTIR spectroscopy. Typical IR vibration spectra of the samples prepared with different HCl dosages are shown in Fig. 1b. In addition to the characteristic adsorption band, the IR spectra characteristic vibrations of defects, which are correlated with the uncoordinated carboxylic group. In detail, the vibration band at 1700 cm-1 corresponds to the C−O vibration of coordinated carboxylic groups and the vibration bands at 1547 cm-1 are representative of the asymmetric and symmetric vibrations of free carboxylic group [43], meanwhile the peak at 747 cm-1 was identified as the formation of Fe−O bond [44]. Control groups with acid coordinators added, the results shown that the IR spectroscopy blue shift of C−O vibration of coordinated carboxyl groups with the weaken peak intensity, indicating that C−O−Fe bond changed with the HCl modulator. On the other hand, the visualization of free carboxyl group indicated that the presence of more uncoordinated ligands due to the absence of the metal clusters dissolved in HCl.

This speculation has been consistent with the weakening of the iron oxide peak located at 747 nm. Compare to free-acid synthesis, the IR band intensity of defect-related band at 1700 cm^{-1} is roughly 1/2 and 1/4 for the modified MOFs with 10 μL HCl and 40 μL HCl, in the synthesis solutions. The similarly decreased peak intensity in equal proportion was reflected in the defect –related Fe−O bands, and it is reasonable to infer that the absence of metal clusters dissolved in HCl modulator is the main cause of the defects.

Nitrogen sorption isotherms of HCl-modulated MIL-53 are shown in Fig. 1c, which are typical I(b) isotherms are reported in the literature for MIL-53. The porosity results are shown in Fig. 1d and the quantitative relationship between the Brunauer-Emmett-Teller (BET) surface area and the dosage can be seen in Fig. 1e. The BET surface area and porosity results and the degree of roughness were shown in Table S1. In the pore size distribution, the appearance of mesoporous structure is the most remarkable feature, in the presence of 10–30 μL, which may be related to the increased photocatalytic activity. Notably, the disappearance of mesoporous structure may contribute to the poor photocatalytic activity of D-4. Similarly, in the facile synthesis of nanosized MIL-101(Cr) with the addition of acetic acid, under too high acetic acid concentration, there is no positive effect for MIL-101(Cr) synthesis, and the by-product MIL-53 showed much lower porosity. In terms of specific surface area, 10 μL HCl played an important role in the increasing the specific surface area. The increase in the specific surface area is noticeable in the presence of 10–30 μL, which may provide more active sites including adsorptive and catalytic ones for photocatalysis. The results were consistent with the study of Shearer [44], the BET surface areas of UiO-66 vary significantly, ranging from 1175 m^2/g (no modulator) to 1777 m^2/g (36Trif), which is one of the highest BET surface areas ever reported for UiO-66 (the current record is 1890 m^2/g).

SEM is the most direct and effective means to characterize materials, as can be seen in Fig. 2, under the action of acid regulation, the crystal change from columnar to double spindle is a remarkable feature. Another remarkable feature is that the appearance of smaller crystals, which were consisted with the XRD diffraction peaks that become wider and shorter. In the study of Huang et al., the irregular morphology existed in the modulated UiO-66 modulated by three alkaline nitrogen heterocycles [45]. In addition, transmission electron microscopy is an important technique to characterization the mesostructure. Because MOFs are generally quite sensitive to the electron beam, it is difficult to obtain highquality images, which was consistent with the study of Zhou
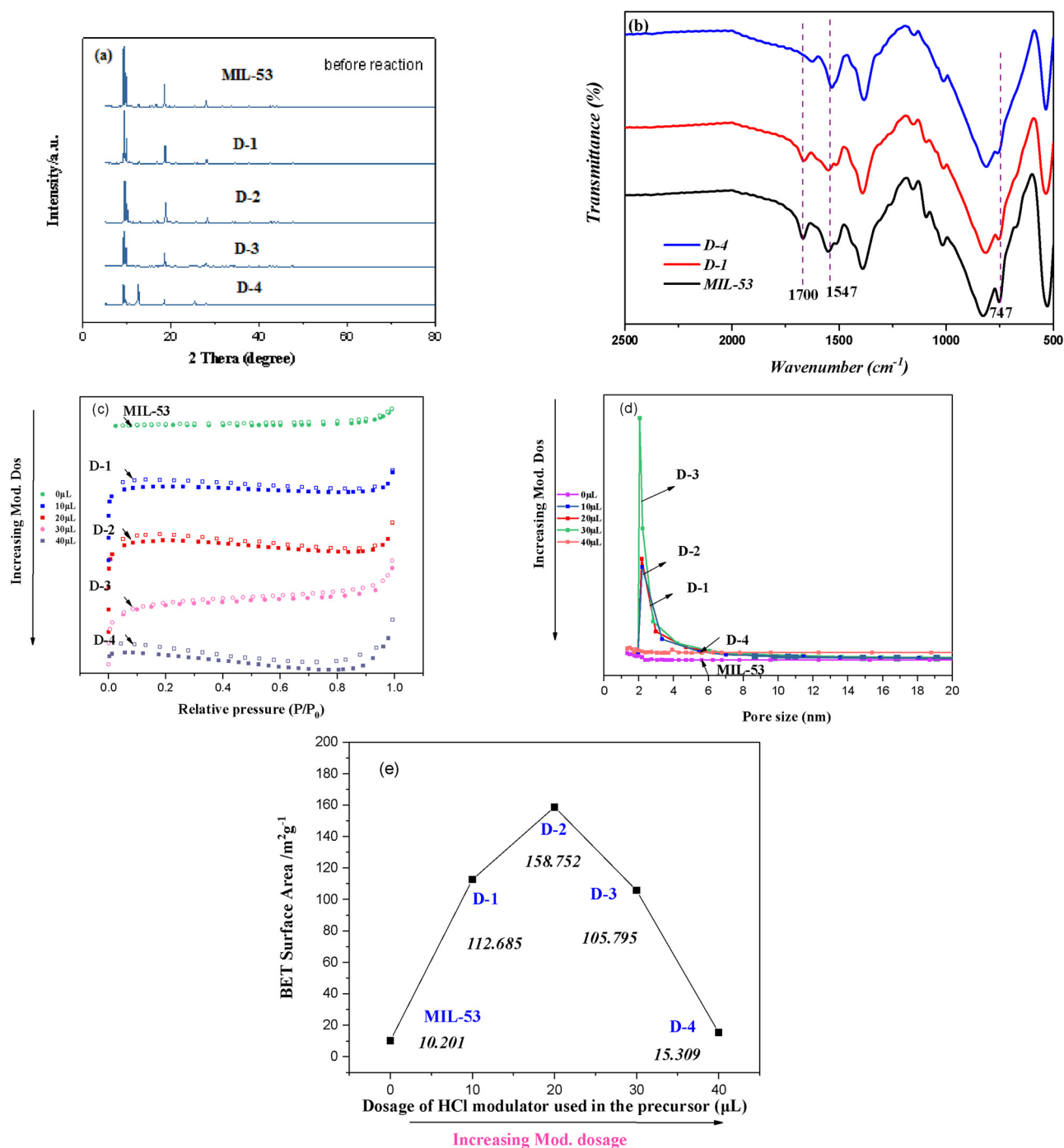
Fig. 1. (a) XRD patterns of MIL-53, D-1, D-2, D-3 and D-4; (b) FTIR spectra of MIL-53, D-1, D-4 ; (c) N_2 absorption-desorption isotherms of MIL-53, D-1 D-2, D-3 and D-4; (d) Pore size distribution of MIL-53, D-1,D-2, D-3 and D-4; (e) Quantitative relationship between amount of HCl and BET surface area.

et al [46]. The mesoporous structures are clearly identified form D-1 and D-4 (Fig. 3).

The surface chemical compositions and states of surface element for MIL-53, D-1 and D-4 were characterized by XPS. The XPS survey spectrum verified that MIL-53 consisted of C, O and Fe. The high re-solution XPS C1 s spectrum in Fig. 4a was fitted into two peaks with the binding energies at 284.4 eV and 288.7 eV, corresponding to the C=C, C−H of the H_2BDC linkers and Fe−COOH functional groups [47]. The acreage ratio of Fe-COOH to C=C and C−H is 0.205 in MIL-53, while in D-1 it decreased to 0.189, then in D-4 it further decreased to 0.174, indicating that the breakage of Fe-O bond was resulted from the ab-sence of the metal clusters. Compared to MIL-53, the red shift occurred

when the binding energy of the two main peaks moved to the higher direction [48].

In the high resolution XPS O 1s spectrum (Fig. 4b), which comprise of two main peaks located in 531.1 eV and 531.9 eV, derived from the oxygen atoms in the carboxylic groups of the H_2BDC linker and the Fe-O bonds of the MIL-53, respectively [49]. Compared to MIL-53, the red shift also occurred when the binding energy of the two main peaks moved to the higher direction. Meanwhile, the acreage ratio of Fe-O to COOH is 0.849 in MIL-53, while in D-1 it decreased to 0.797, then in D-4 it further decreased to 0.754, indicating that the share is shrinking attributed to the defect of metal clusters. XPS is helpful in analyzing the crystal defects. XPS peak position and strength contributed to the
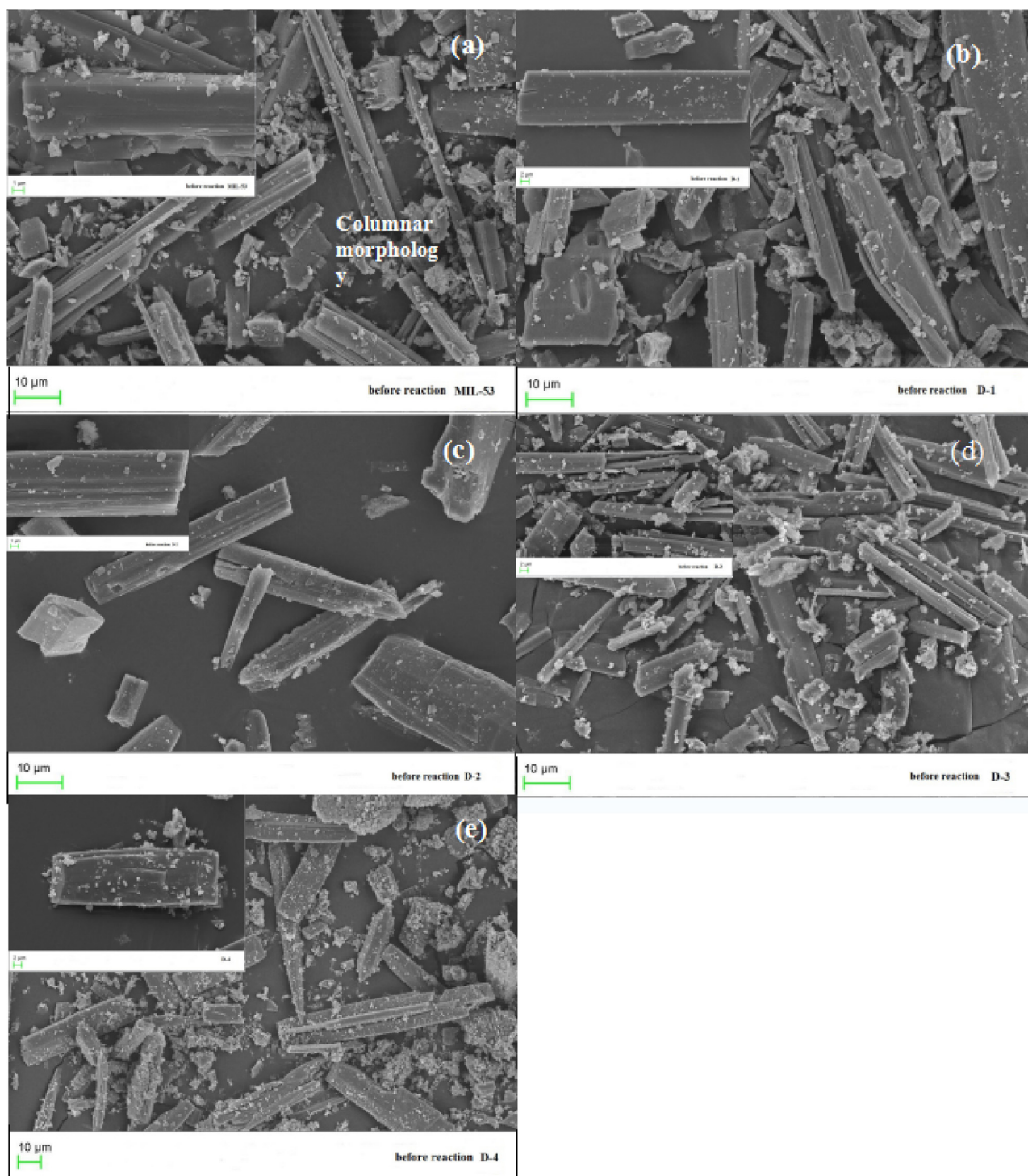
Fig. 2. SEM images of (a) MIL-53; (b) D-1; (c) D-2,(d) D-3;(e) D-4.

analysis of the coordination environment of metal clusters and ligands. In the study of Xuan [50], the defect sites of Trifluroacetic acid (TFA) modulated UiO-66 was studied by XPS. The high resolution Zr 3d spectra of UiO-66-X are studied. The spectra of Zr 3d could be deconvoluted into two peaks. The peak at ~182.8 eV can be assigned to Zr $3d_{5/2}$ of the zirconium atoms in Zr6 clusters, and the peak at ~185.1 eV can be ascribed to Zr $3d_{3/2}$ of the zirconium atoms in missing-linker defects (Zr^{4+}, Zr–OH_2 and Zr–OH). It can be seen that the increased amount of TFA decreased the proportion of Zr $3d_{5/2}$ and increase the proportion of Zr $3d_{3/2}$ due to the increased missing-linker defects in UiO-66-X. Besides, compare to UiO-66-O, both the binding energy of

Zr3d $_{5/2}$ and Zr 3d $_{3/2}$ for UiO-66-X synthesized with TFA modulation shift to lower value. In our work, the XPS peak position and peak strength of the Fe 2p were slightly affected by the trace acid (Fig. 4c), the significant effect was exhibited by 40 μL HCl may be due to the changed coordination environment of Fe from MIL-53 to MIL-88. Meanwhile, for binding energy, the red shift indicates that the coordination bond of Fe-O changes. The FTIR combine with the XPS analysis confirmed that the defect was caused by the sacrifice of the metal clusters.

Therefore, acid regulation strategy has a great influence on the structure and morphology of MIL-53. Structurally, the crystal growth
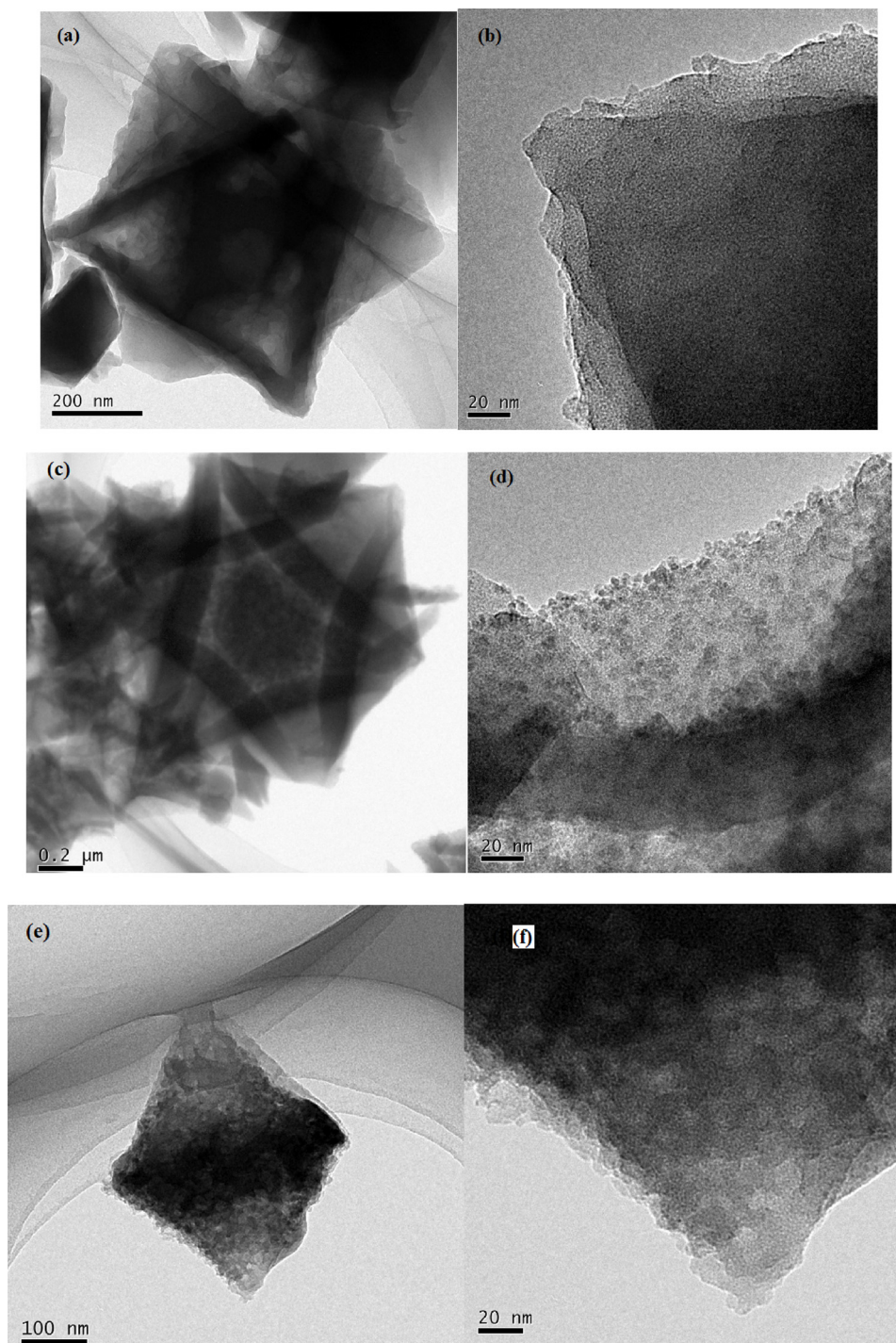
Fig. 3. TEM images of MIL-53(a,b); D-1 (c,d); D-2 (e,f).

was inhibited by 10 μL HCl treatment and then smaller crystals were obtained; however, layer crystal structure regulated by 40 μL HCl exhibited. Due to the contribution of HCl regulator, the increased specific structure and the pore structure transformed from microporous to mesoporous structure. It is essential to confirm the defect of the metal clusters from the FTIR and XPS analyses. These changes in structural may have an effect on their properties, such as the photoelectric properties, and they got further exploration.

3.2. Photocatalytic activity of MIL-53 and D-MIL-53 (Fe)

3.2.1. Different photocatalytic activity

Due to the widespread existence and perniciousness of organic pollution, antibiotic wastewater by virtue of degradation-resistant was selected as the study object to evaluate the photocatalytic activity of different materials [51–53]. Depicted in Fig. 5a shows the comparison of TC removal efficiency on photocatalysts MIL-53 and D-MIL-53 (D-1 - D-10). Obviously, all the samples could adsorb TC to some degree in the darkness, which was due to the good adsorption ability of MOFs with mesoporous structure [54]. As a typical porous material, adsorption property of MOFs could not be ignored. Both the adsorption and the
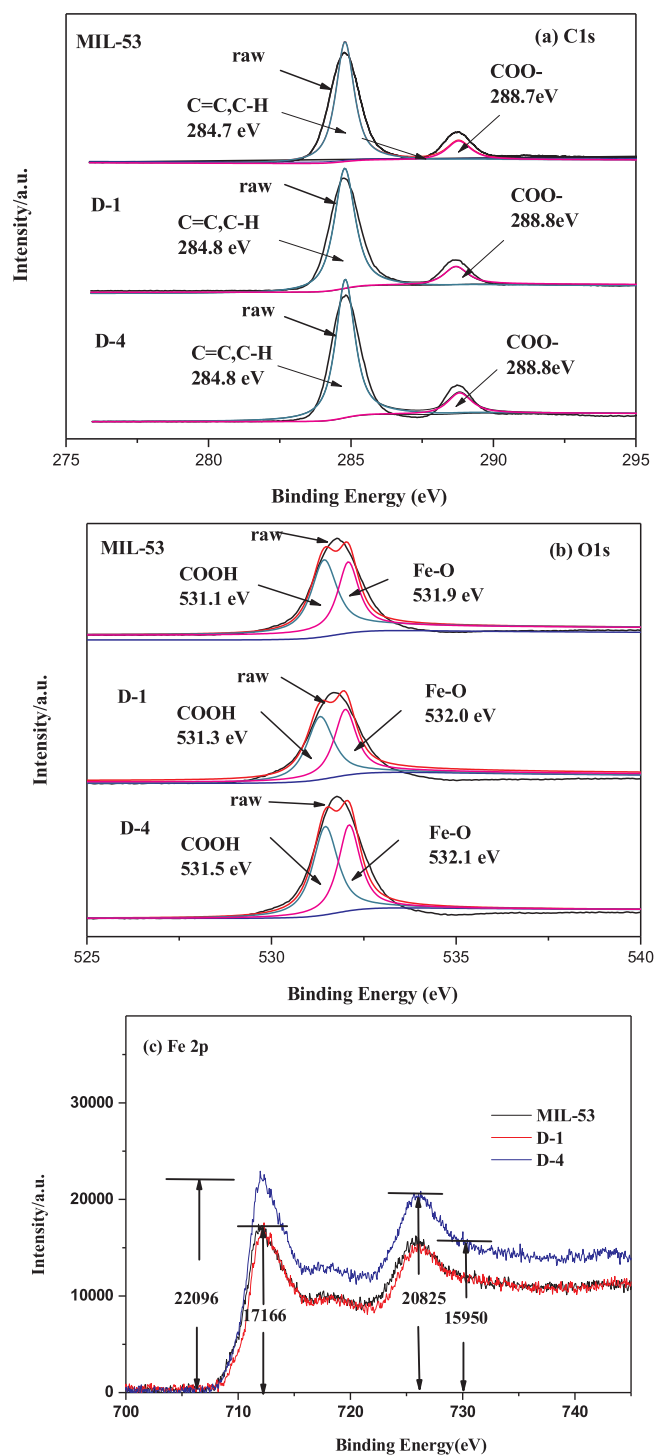
Fig. 4. XPS Spectra of the MIL-53, D-1 and D-4 (a) C 1s of MIL-53, D-1 and D-4; (b) O 1s of MIL-53, D-1 and D-4; (3) Fe 2p of MIL-53, D-1 and D-4.

photocatalytic capacity were improved of D-1, D-2 and D-3. The increased adsorption capacity was due to the contribution of increased specific surface area and pore volume, which was consistent with the previous BET characterization. The photocatalytic degradation efficiency of MIL-53 was 60.1%, however, small amount of HCl (10 μL, 20 μL and 30 μL) could dramatically improve the photocatalytic activity (90.1%, 79.2% and 69.2%). Notably, the photocatalytic activity of D-1 was 1.5 times enhanced compared to that of MIL-53. On the other hand, the photocatalytic degradation efficiency was reduced to 52%, 42% and 37% when further adding 40 μL, 50 μL, 100 μL HCl into precursor

solution. HCl over 40 μL exhibited negative impact on the photocatalytic performance, indicating that the amount of acid modulator affected the photocatalytic activity of materials. In addition, the quantitative relationship between the photocatalytic activities the photocatalyst and the modulators are as shown in Fig. 5b. Furthermore, regular linear results exhibited by the plots of $-\ln(C_t/C_0)$ *versus* irradiation time (t) indicated that photocatalytic process followed the first order kinetic equation [55]. The photocatalytic activities of different materials were analyzed and the reaction kinetic constants of different photocatalysts were calculated. The datas in Fig. 5 were fitted, the calculated first-order reaction kinetic constants were 0.01042, 0.00701, 0.00556, 0.004 and 0.00338, and the corresponding correlation coefficients (R^2) were 0.96232, 0.97312, 0.96866, 0.93659, 0.95528. Compared with MIL-53, the reaction rates of D-1, D-2, D-3 and D-4 were increased by 2.6, 1.8, 1.4 and 0.85 times. The results showed that the acid is sensitive in enhanced photocatalytic reactivity.

3.2.2. The effect of initial TC concentrations

Actually, the concentration of TC varies largely in the natural environment, and high concentration of wastewater may have passivation effect on photocatalysts. Thus, it is essential to discuss the effect of initial TC concentration on the photocatalytic performance of the photocatalyst. Based on the above results, the D-1 by virtue of its excellent photocatalytic activity was selected as the research object and the response of different concentration antibiotic wastewater was studied. Fig. 5c displayed the effect of different initial TC concentration on the degradation efficiency of D-1. Obviously, it can be seen that the degradation rate is affected by the initial concentration to some extent. D-1 has the best removal results for the degradation of 10 mg/L TC wastewater and almost complete degradation was achieved (96.9%). The removal efficiencies of TC declined to 79.1% when the initial TC concentration increased to 40 mg/L. It may be that dense tetracycline molecules restric light transmition. The adsorption sites are competed by parent molecules and intermediates, which leads to low photocatalytic efficiency [56,57].

3.2.3. The removal efficiency of total organic carbon (TOC)

The variation of the total organic carbon (TOC) was used to measure the degree of mineralization of photocatalytic degradation pollutants. As shown in **Fig. S1**, the TOC removal efficiencies for the D-4, MIL-53 and D-1 were 12.3%, 18.7% and 21.9% under 30 min light exposure, when the light increased to 150 min., the TOC removal efficiencis increased to 39.8%, 50.5% and 61.3%. The results demonstrate that the defective MIL-53, based on he mineralization ability, has good photocatalytic activity. The identification of intermediates and inference of photocatalytic degradation pathway based on mineralization process was aided by LC–MS/MS and 3D EEMs.

3.2.4. Possible photocatalytic degradation pathway of TC

The pathway of photocatalyic degradation was clarified in the process of photocatalytic degradation. The degradation intermediates of TC in the presence of D-1 were identified by LC-MS/MS, as shown in **Fig. S2**. Based on the detected intermediates, the photocatalytic degradation pathway was speculated as shown in **Fig. S3**. The generated intermediate TC 1 was attributed to the reaction of TC deamidation, while the transformation from TC 1 to TC 2 was based on the loss of dimethylamino group. Then the TC 2 was fragmented into TC 3 through a series of transformations, including dehydroxylation, opening rings of benzene, deethylation and additional reaction. In the end, the deacetylation and oxidation reaction was responsible for the change from TC 3 to TC 4. The presumed photocatalytic degradation pathway was consistent with that of Yang et al. by Ag@AgI/V_I-BOI photocatalyst [58].

Additional, 3D EEMs can also explain the TC degradation pathway to a certain extent. As revealed in **Fig. S4 (a) and (b)**, there was no significant difference the original solution and the solution obtained
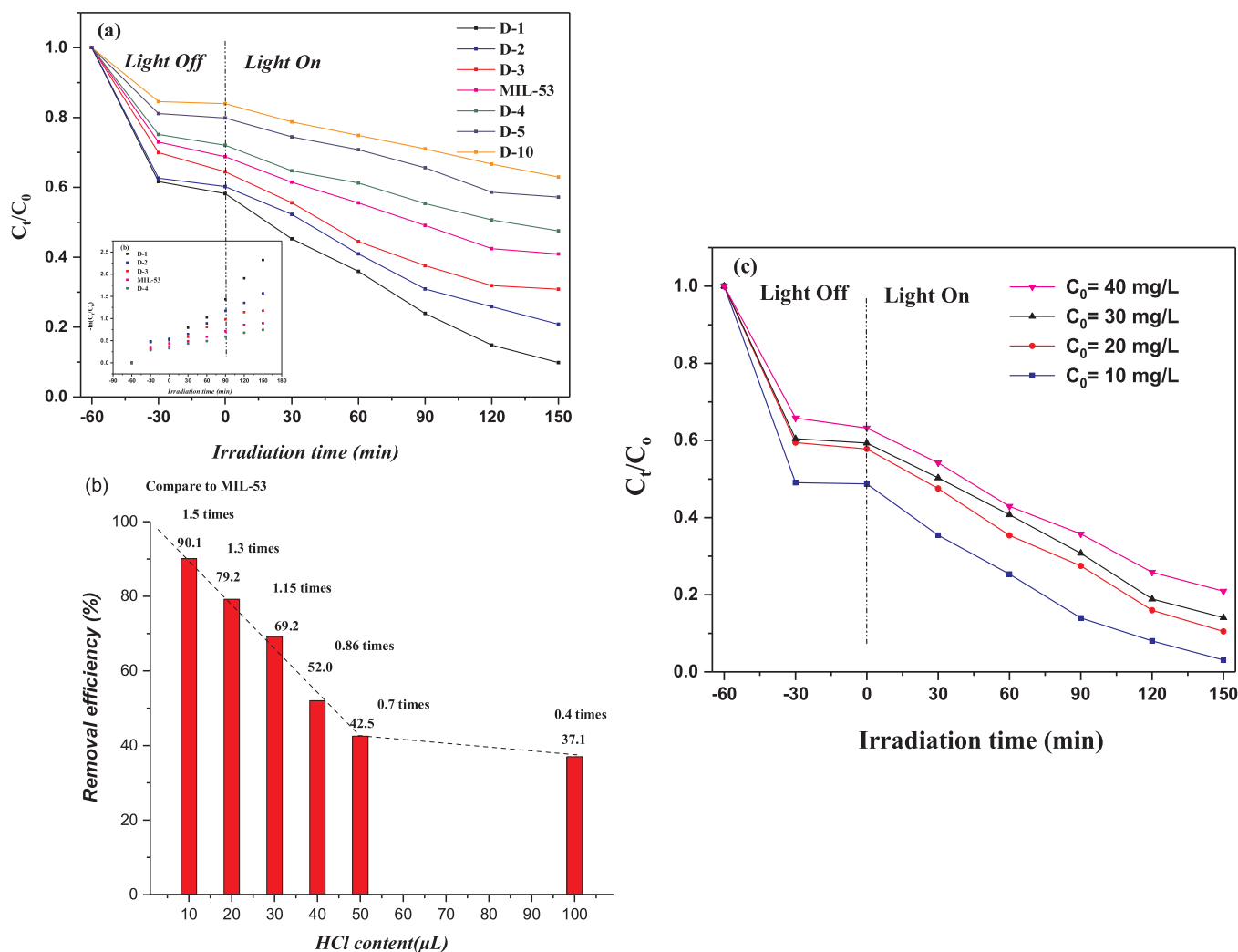
Fig. 5. (a) The different photocatalytic activity of MIL-53, D-1, D-2, D-3, D-4, D-5 and D-10; (b) (inner) Kinetic curves of TC degradation by MIL-53, D-1, D-2, D-3 and D-4; (b) The qualitative relationship between different of HCl content and the removal efficiency; (c) The impact of initial TC concentration on D-1.
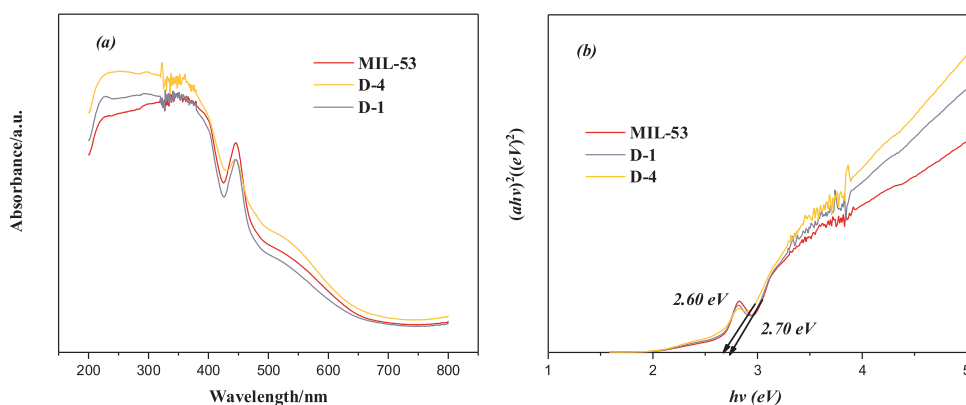

Fig. 6. (a) UV–vis light spectra of MIL-53, D-1 and D-4; (b) Band-gap of MIL-53, D-1 and D-4.

after 60 min dark adsorption, suggesting that in the dark reaction stage, adsorption played a leading role. Conversion conditions to provide a visible light source, the fluorescence peak located at λex/λem = (340–350 nm)/(500–510 nm) and λex/λem = (335–345 nm)/(495–505 nm) appeared **Fig. S4 (c)**, suggesting the structure of intermediate products are similar to the fulvic acid and humic acid [59,60]. With the passage of time to 150 min **Fig. S4 (d)**, the photocatalytic degradation has been confirmed in depth by the deepen intensity of the

fluorescence peak, and the results are consistent with the inferred photocatalytic degradation pathway. And the intermediates may evolve further into CO_2 and H_2O.

3.2.5. Reusability and stability

The reusability and stability of materials are important for practical application. As shown in **Fig. S5**, compared to 90.1% degradation efficiency of D1 under the 20 mg/L, it reduced to 74.3% after four times
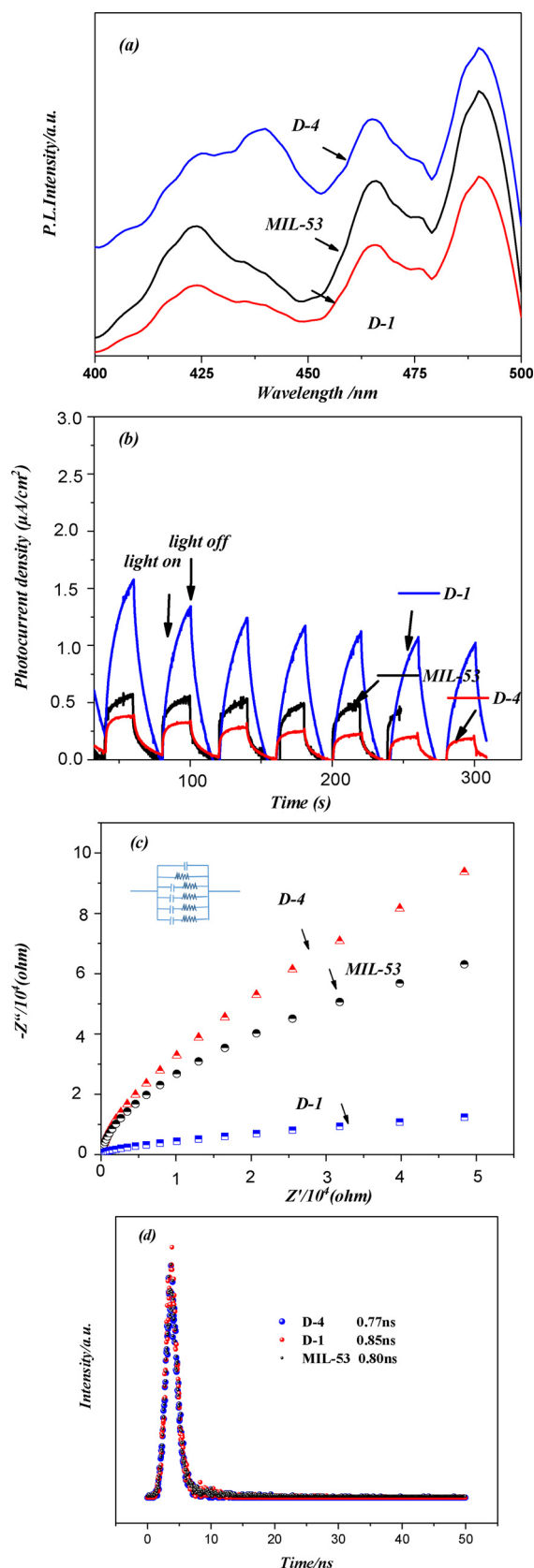
Fig. 7. The photoelectric characterization (a) Photoluminescence spectra for MIL-53, D-1 and D-4; (b) Transient photocurrent responses of MIL-53, D-1 and D-4; (c) EIS Nyquist plots of MIL-53, D-1 and D-4;(d) Transient fluorescence lifetime of MIL-53, D-1 and D-4.

recycle, suggesting that the modulated MOFs was stable and reusable. Good stability and reusability are important guarantees for practical application. Interestingly, as can be seen in **Fig.S6** the diffraction of XRD changed obviously after photocatalytic reaction, the diffraction of which was consistent with MIL-88 [61], indicating that irradiation is the driving force of crystal transformation. In the study of Nguyen etal [62]., the photocatalytic activities of MIL-88 and that of MIL-53 were compared, it of MIL-88 was slightly lower than that of MIL-53. This also explains why MIL-53 photocatalytic activity decreases after several cycles, and the key to the problem lies in the crystal transformation.In the study of Zhou, in the preparation of CTAB/CA (CTAB, cetyl-trimethylammonium bromide; CA, citric acid) modulated $Cu_2(BTC)_3$, for the samples synthesized with high CTAB/CA ratios, their X-ray diffraction patterns are in good agreement with that reported for $Cu_2(BTC)_3$. Nonetheless, an excess amount of CA favors the generation of a new crystalline phase with a typical diffraction line at $2\theta = 10.1°$. The incorporation of excessive CA into frameworks should be responsible for the new phase. However, the formation of composite photocatalyst can increase the stability of MIL-53, such as Ag_3PO_4/MIL-53 [63], SnS/MIL-53 [64], the stability of photocatalyst was confirmed by the diffraction peaks that remained consistent before and after the reflection. In addition, we provided the SEM images after degradation, which was important to analyze the mechanism and stability of photocatalytic degradation. As can be seen in **Fig. S7,** after the reaction, the most remarkable feature is the appearance of many regular hexahedral crystals, which represented the typical structure of MIL-88 and were consisted with the XRD characterization.

3.3. Mechanism of different photocatalytic activity

The optical properties play important roles in assessing the photocatalytic abilities for photocatalysts. The light-absorption property of MIL-53, D-1 and D-4 were tested through the UV–vis DRS measurements. As shown in Fig. 6a, MIL-53, including the perfect and modulated types, displayed a strong absorption within the visible light range, signifying their potential capacity for visible-light harvesting [65]. In the UV–vis DRS spectrum of MIL-53, the absorption peak at 445 nm, it of D-1 and D-4 are similar with that of MIL-53, which was attributed to the spin-allowed d-d transition ($[^6A_{1g} \rightarrow 4A_{1g} + {}^4Eg(G)]$) of Fe^{3+} in MOFs [67]. Similar band gap of MIL-53, D-1 and D-4 located at 2.70 eV, 2.70 eV, 2.60 eV (Fig. 6b), based on the relation of Eg = 1240/λ, which were similar to the existing findings. In the study of Du et al. [35], it can be observed that the absorption edge of the as-prepared MIL-53(M) photocatalysts is gradually shifted to longer wavelength by altering metal ions from Al to Cr and to Fe. The onset of the main absorption edge of MIL-53 (Al), MIL-53 (Cr) and MIL-53 (Fe) was 320 nm, 395 nm and 455 nm, which corresponds to the band gaps (Eg) of 3.87, 3.20 and 2.72 eV (Eg = 1240/wavelength). In the study of Nguyen *et al.* [66], the MIL-53(Fe) samples show the strong absorption bands in the range of 200–450 nm, which can be assigned to absorption induced by ligand-to-metal charge transfer (LMCT) of O (II)→ Fe(III). A band gap of MIL-53(Fe) was estimated to be 2.72 eV. In addition, in the study of Liang *et al.* [67], the main optical absorption edge of MIL-53-0.5% RGO is estimated to be 455 nm. Based on the relation Eg = 1240/λ, the calculated optical band gap of which is 2.72 eV. Other similar work has been reported in the study of Bai et al. [37], Lin et al. [68], and Gao et al. [69]. Considering the photoactivity, the band gap may not be the main factor affecting the photocatalytic activity.

The separation of photocarriers related with photocatalytic activity was analyzed from three aspects:(1) Photoluminescence (PL) emission was considered as a reference for the separation system of photogenic carriers [70]. Generally, a lower PL intensity corresponding to a high photocatalytic activity was due to the enhanced photo-excited electron-hole pairs separation efficiency [71]. Fig. 7a revealed the differences on the PL spectra of MIL-53, D-1 and D-4 under an excitation wavelength of 340 nm. Upon photoexcitation at 340 nm, the MIL-53 photocatalyst
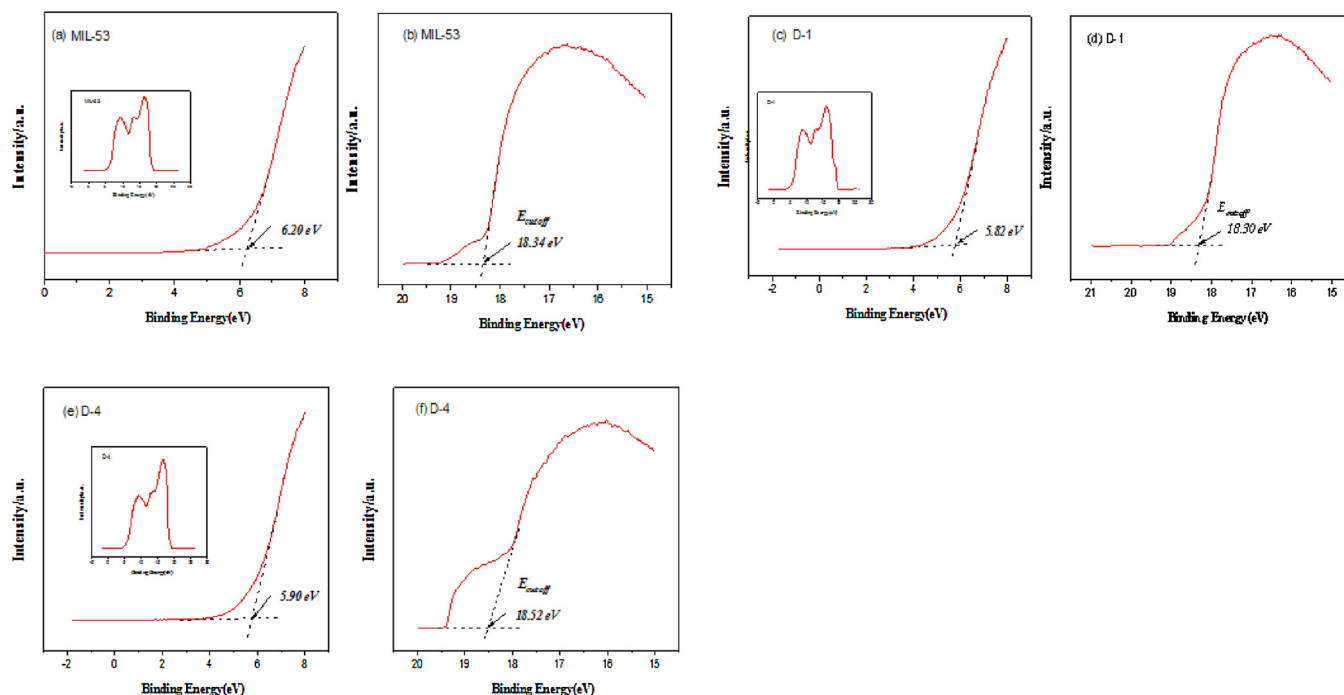
Fig. 8. UPS spectra of (a) MIL-53; (c) D-1; (e) D-4; and the cutoff energy (Ecutoff) of MIL-53 (b), D-1 (d) and D-4 (f).
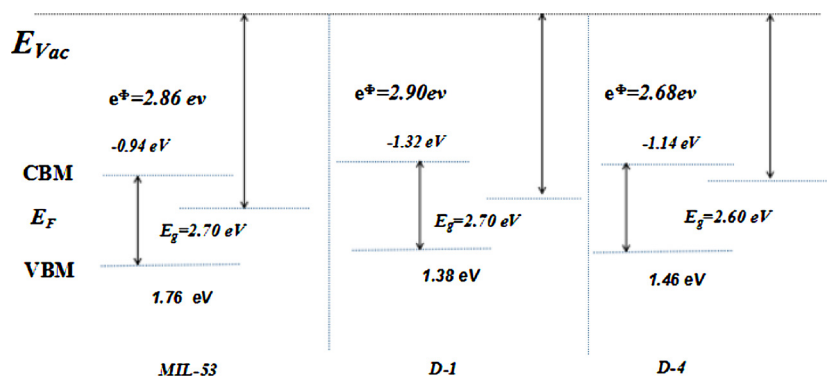

Fig. 9. The energy level structure of MIL-53, D-1 and D-4.

exhibited a broad band at 400–500 nm with peaks at 425 nm, 465 nm and 490 nm, respectively. The reduced PL intensity of D-1, compared to the MIL-53, indicated the delayed combination of photo-induced electron-hole pairs due to the HCl modualtor. At the same time, there was a significant red shift. Meanwhile, the deformation of photoluminescence spectrum may be related to the structural change of D-4. (2) Photocurrent (PC) represents the migration of photogenic carriers. As shown in Fig. 7b, the photocurrent of the D-1 is the most prominent, indicating that the fast separation rate of photo-excited charges was controlled by defect. This may be the defect sites as a traps to capture the generated electrons and holes, resulting in the prolonged the charge carriers lifetime [72]. Besides, Fig. 7c showed the EIS analysis. it is obvious that the relative size of art is in the order of D-4 > MIL-53 > D-1, suggesting that defective MIL exhibited a more efficient charge separation and electron transfer ability. In addition, simulated equivalent circuit of impedance analysis was shown in Fig. S8, and the fitting degree values of D-1, MIL-53 and D-4 are $2.32E^{-3}$, $2.17E^{-3}$, $3.49E^{-3}$, respectively. Combining all the optical representations, the defect strategy by acid modulator can regulate the optical properties. To illustrate the separation and recombination of photogenic carriers, we further tested the fluorescence lifetime of the materials including D-1, D-4 and MIL-53,as shown in Fig. 7d. Refer to multi-exponential fitting, the

fluorescence lifetimes of MIL-53, D-1 and D-4 were 0.80 ns, 0.85 ns, 0.77 ns, and the results showed that acid regulation prolongs the life of the photogenic carriers. The reduced fluorescence life of D-4 was attributed to the changed crystal form from MIL-53 to MIL-88. The increase of fluorescence lifetime makes photogenic carriers more likely to participate in photocatalytic reaction before recombination.

It is necessary to determine the VBM of the samples by UPS, and accurate information was provided to determine the energy level structure of the material. The bandgap energy (Eg) of MIL-53, D-1 and D-4 were determined to be 2.70 eV, 2.70 eV and 2.60 eV, respectively. Next, ultraviolet photoelectron spectroscopy (UPS) provides a basis for determining the energy level structure. As shown in Fig. 8 the valence band energy (ECB) were 6.20 eV, 5.82 eV, 5.90 eV for MIL-53, D-1 and D-4. Moreover, the cutoff energy (Ecutoff) of MIL-53, D-1 and D-4 are 18.34 eV, 18.30 eV and 18.52 eV on the basis of fermi level (E_f) are 0 eV. According to the following equation, $e\Phi = hv - | Ecutoff - Ef |$, their work function ($e\Phi$) were equal to 2.86 eV, 2.90 eV and 2.68 eV,as shown in Fig. 9. The transport of photogenic carriers is driven by larger work function, thus, the high photocatalytic activity may be related to the large work function. In addition, the VB can be determined by virtue of XPS, as shown in Fig.S9. The VB of MIL-53, D-1 and D-4 are 1.60 eV,1.60 eV and 1.50 eV, the results showed that the two
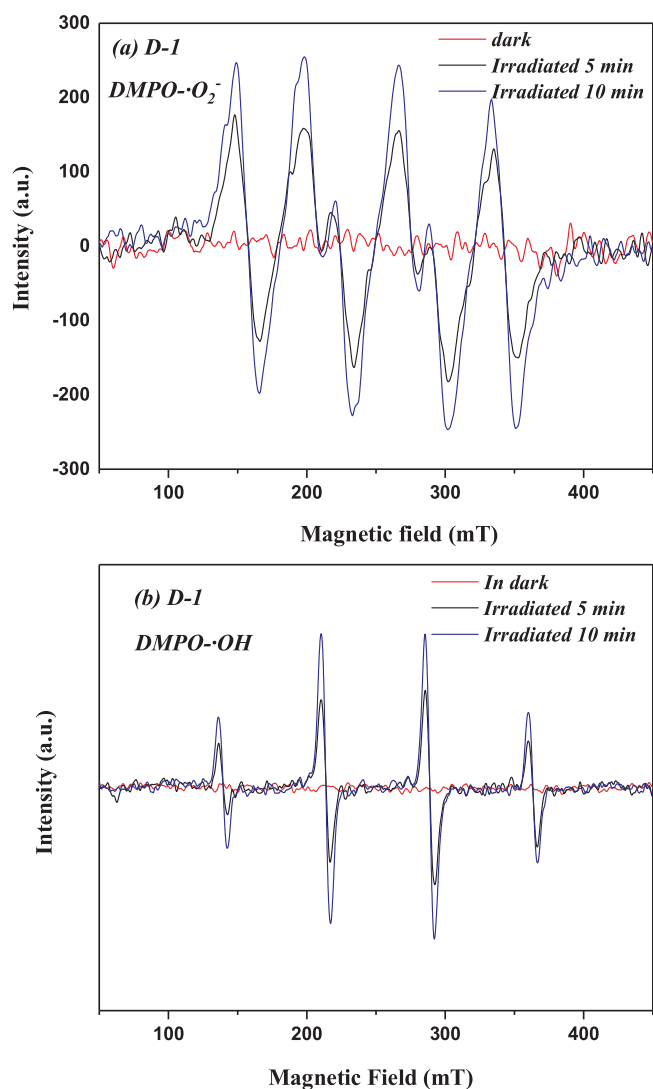
Fig. 10. The active drivers associated with the photocatalytic process in D-1 (a) O_2^- ;(b) OH.

technologies including UPS and XPS-VB used different light sources and the values are highly similar.

Free radicals provide the power for photocatalytic reactions and some oxygen-containing such as $\cdot O_2^-$ (superoxide radicals) and $\cdot$OH (hydroxyl radicals) have been confirmed in free radicals capture experiments. For D-1 with the highest photocatalytic activity, there was no signal under dark conditions, instead, the signal peak with equal spacing of 1: 1: 1: 1 appeared at 5 min and was considered to be $\cdot O_2^-$, as shown in Fig. 10a. Attributed to the more negative reduction potential of $O_2/\cdot O_2^-$ (-0.33 eV vs NHE), it makes it impossible for O_2 to react with the electrons on the CB of D-1 to the generation of $\cdot O_2$-. The signal peak was strengthened, when increasing time to 10 min., indicating that more active $\cdot O_2^-$ were generated. The change trend of $\cdot O_2$- was consisted with that of the TC degradation, indicating that they were the driving force of photocatalytic degradation. The similar trend was observed in the MIL-53 (**Fig. S10a**) and D-4(**Fig. S10c**).

On the other hand, the signal peak with equal spacing of 1:2:2:1 was deemed as the signal peak of $\cdot$OH. As show in Fig. 10b, the characteristic signals of $\cdot$OH could be ignored in dark while it appeared at 5 and 10 min. The generation of $\cdot$OH mainly comes from two aspects: (1) The reduction of $\cdot O^{2-}$ via the routes of $\cdot O^{2-} \rightarrow H_2O_2 \rightarrow \cdot OH$, as the VB potential (2.36 eV vs NHE) of D-1 was less then the oxidation potential of OH-/$\cdot$OH (2.40 eV vs NHE), which failed to oxidize the H_2O surface or

OH- to form $\cdot$OH; (2) H_2O_2 generated from the electrons reaction with dissolved O_2 and H^+, then which could be further transformed to generate $\cdot$OH as reaction: e_{CB}- + $H_2O_2 \rightarrow \cdot OH + OH$- [73], indicating that $\cdot$OH as another important driver propel the photocatalytic reactions. The similar trend was observed in the MIL-53 (**Fig. S10b**) and D-4 (**Fig. S10d**). Thus, $\cdot O^{2-}$ and $\cdot$OH are provided by modulated MOFs as driving forces to demineralize the organic pollutants.

4. Conclusions

It is interesting and meaningful to application of HCl-modulated MIL-53 for the photocatalytic degradation of organic pollutants, providing another possibility for the removal of organic pollutants. The effect of acid modulator on structure and the photocatalytic activity were emphasically investigated. Structurally, the increased specific surface and new mecroporous structures caused by acid modulator may be related with the defects due to the absence of metal clusters. The differences in properties, in particular, the photocatalytic properties affected by the differences in structure. Compare with MIL-53, the photocatalytic activity of acid-regulated MIL-53 increased by 1.5 times due to the easier separation of photogenerated carriers, in addition, the quantitative relationship between the content of modulator and the photocatalytic activity was revealed. Good recycling until the fourth cycles is an important guarantee for reuse. In addition, form the ERP analysis, $\cdot O_2^-$ and $\cdot$OH are provided by modulated MOFs as driving forces to demineralize the organic pollutants.

Acknowledgements

Appendix A. Supplementary data

Supplementary material related to this article can be found, in the online version, at doi:https://doi.org/10.1016/j.apcatb.2019.117746.

References

[1] D.N. Jiang, P. Xu, H. Wang, G.M. Zeng, D.L. Huang, M. Chen, C. Lai, C. Zhang, J. Wan, W.J. Xue, Coord. Chem. Rev. 376 (2019) 471–483.
[2] H.L. Jiang, Q. Xu, Chem. Commun. 47 (2011) 3351–3370.
[3] Z.L. Fang, B. Bueken, D.E. De Vos, R.A. Fischer, Angew. Chem.-Int. Edit. 54 (2015) 7234–7254.
[4] D.N. Jiang, P. Xu, H. Wang, G.M. Zeng, D.L. Huang, M. Chen, C. Lai, C. Zhang, J. Wan, W.J. Xue, Coord. Chem. Rev. 376 (2018) 449–466.
[5] M. Cheng, C. Lai, Y. Liu, G.M. Zeng, D.L. Huang, C. Zhang, L. Qin, L. Hu, C.Y. Zhou, W.P. Xiong, Coord. Chem. Rev. 368 (2018) 80–92.
[6] H. Wang, X.Z. Yuan, Y. Wu, G.M. Zeng, H.R. Dong, X.H. Chen, L.J. Leng, Z.B. Wu, L.J. Peng, Appl. Catal. B-Environ. 186 (2016) 19–29.
[7] H. Wang, X.Z. Yuan, Y. Wu, G.M. Zeng, X.H. Chen, L.J. Leng, H. Li, Appl. Catal. B-Environ. 174 (2015) 445–454.
[8] S. Dissegna, K. Epp, W.R. Heinz, G. Kieslich, R.A. Fischer, Adv. Mater. 30 (2018) 23.
[9] C.A. Trickett, A. Helal, B.A. Al-Maythalony, Z.H. Yamani, K.E. Cordova, O.M. Yaghi, Nat. Rev. Mater. 2 (2017) 16.
[10] D.B. Wang, F.Y. Jia, H. Wang, F. Chen, Y. Fang, W.B. Dong, G.M. Zeng, X.M. Li, Q. Yang, X.Z. Yuan, J. Colloid Interface Sci. 519 (2018) 273–284.
[11] Z. Fang, B. Bueken, D.E. De Vos, R.A. Fischer, Angew. Chem.-Int. Edit. 54 (2015) 7234–7254.
[12] M. Taddei, R.J. Wakeham, A. Koutsianos, E. Andreoli, A.R. Barron, Angew. Chem.-Int. Edit. 57 (2018) 11706–11710.
[13] H. Furukawa, U. Muller, O.M. Yaghi, Angew. Chem.-Int. Edit. 54 (2015) 3417–3430.

[14] G.C. Shearer, S. Chavan, S. Bordiga, S. Svelle, U. Olsbye, K.P. Lillerud, Chem. Mater. 28 (2016) 3749–3761.
[15] P.Á. Szilágyi, P. Serra-Crespo, I. Dugulan, J. Gascon, H. Geerlings, B. Dam, CrystEngComm 15 (2013) 10175.
[16] H. Wu, Y.S. Chua, V. Krungleviciute, M. Tyagi, P. Chen, T. Yildirim, W. Zhou, J. Am. Chem. Soc. 135 (2013) 10525–10532.
[17] W.M. Gao, D.Z. Chen, H.Y. Quan, R. Zou, W.X. Wang, X.B.A. Luo, L. Guo, ACS Sustain. Chem. Eng. 5 (2017) 4144–4153.
[18] W.B. Liang, L. Li, J.W. Hou, N.D. Shepherd, T.D. Bennett, D.M. D'Alessandro, V. Chen, Chem. Sci. 9 (2018) 3508–3516.
[19] L. Zeng, L. Xiao, Y.K. Long, X.W. Shi, J. Colloid Interface Sci. 516 (2018) 274–283.
[20] T. Liu, Y.X. Liu, L.L. Yao, W.X. Yang, L. Tian, H.L. Liu, D. Liu, C. Wang, Nanoscale 10 (2018) 13194–13201.
[21] X. Mu, Y. Chen, E. Lester, W. Tao, Microporous Mesoporous Mater. 270 (2018) S1387181118302798.
[22] E. Bagherzadeh, S.M. Zebarjad, H.R.M. Hosseini, Eur. J. Inorg. Chem. (2018).
[23] C. Atzori, G.C. Shearer, L. Maschio, B. Civalleri, F. Bonino, C. Lamberti, S. Svelle, K.P. Lillerud, S. Bordiga, J. Phys. Chem. C 121 (2017) 9312–9324.
[24] G. Cai, H.-L. Jiang, Angew. Chem.-Int. Edit. 56 (2017) 563–567.
[25] Q. Xia, B. Huang, X. Yuan, H. Wang, Z. Wu, L. Jiang, T. Xiong, J. Zhang, G. Zeng, H. Wang, J. Colloid Interface Sci. 530 (2018) 481–492.
[26] M.J. Pu, Z.Y. Guan, Y.W. Ma, J.Q. Wan, Y. Wang, M.L. Brusseau, H.Y. Chi, Appl. Catal. A-Gen. 549 (2018) 82–92.
[27] P. Shukla, I. Fatimah, S. Wang, H.M. Ang, M.O. Tadé, Catal. Today 157 (2010) 410–414.
[28] C.H. Zhang, L.H. Ai, J. Jiang, J. Mater. Chem. A 3 (2015) 3074–3081.
[29] W. Mei, D.Y. Li, H.M. Xu, J. Zan, L. Sun, Q. Li, B.Y. Zhang, Y.F. Wang, D.S. Xia, Chem. Phys. Lett. 706 (2018) 694–701.
[30] Y. Han, C. Bai, L. Zhang, J. Wu, H. Meng, J. Xu, Y. Xu, Z. Liang, X. Zhang, New J. Chem. 42 (2018) 3799–3807.
[31] X.Q. Hao, Z.W. Cui, J. Zhou, Y.C. Wang, Y. Hu, Y. Wang, Z.G. Zou, Nano Energy 52 (2018) 105–116.
[32] Y. Hau, L. Zhang, C. Bai, J. Wu, H. Meng, Y. Xu, Z. Liang, Z. Wang, X. Zhang, Appl. Organomet. Chem. 32 (2018) e4325.
[33] F.A. Sofi, K. Majid, Mater. Chem. Front. 2 (2018) 942–951.
[34] W.P. Xiong, Z.T. Zeng, X. Li, G.M. Zeng, R. Xiao, Z.H. Yang, Y.Y. Zhou, C. Zhang, M. Cheng, L. Hu, C.Y. Zhou, L. Qin, R. Xu, Y.R. Zhang, Chemosphere 210 (2018) 1061–1069.
[35] J.J. Du, Y.P. Yuan, J.X. Sun, F.M. Peng, X. Jiang, L.G. Qiu, A.J. Xie, Y.H. Shen, J.F. Zhu, J. Hazard. Mater. 190 (2011) 945–951.
[36] D. Wang, F. Jia, H. Wang, F. Chen, Y. Fang, W. Dong, G. Zeng, X. Li, Q. Yang, X. Yuan, J. Colloid Interface Sci. 519 (2018) 273–284.
[37] E. Bagherzadeh, S.M. Zebarjad, H.R.M. Hosseini, Eur. J. Inorg. Chem. (2018) 1909–1915.
[38] E.S. Sanil, K.-H. Cho, S.-K. Lee, et al., J. Porous Mater. 22 (1) (2014) 171–178 2014.
[39] T. Zhao, L. Yang, P.Y. Feng, et al., Inorg. Chim. Acta 471 (2018) 440–445.
[40] L. Yang, T. Zhao, I. Boldog, et al., Dalton Trans. 48 (3) (2019) 989–996.
[41] S.K. Patra, S. Rahut, J.K. Basu, New J. Chem. 42 (2018) 18598–18607.
[42] Y.D. Han, H.L. Shi, C.P. Bai, L.X. Zhang, J.B. Wu, H. Meng, Y. Xu, X. Zhang, Chemistryselect 3 (2018) 8045–8050.
[43] D. Guo, R.Y. Wen, M.M. Liu, H.X. Guo, J.H. Chen, W. Weng, Appl. Organomet. Chem. 29 (2015) 690–697.
[44] W. Xiong, G. Zeng, Z. Yang, Y. Zhou, C. Zhang, M. Cheng, Y. Liu, L. Hu, J. Wan, C. Zhou, R. Xu, X. Li, Sci. Total Environ. 627 (2018) 235–244.
[45] T. Liu, Y.X. Liu, L.L. Yao, W.X. Yang, L. Tian, H.L. Liu, D. Liu, C. Wang, Nanoscale 10 (2018) 13194–13201.
[46] L.C. Xie, Z.H. Yang, W.P. Xiong, Y.Y. Zhou, J. Cao, Y.R. Peng, X. Li, C.Y. Zhou, R. Xu, Y.R. Zhang, Appl. Surf. Sci. 465 (2019) 103–115.
[47] A.S. Huang, L.L. Wan, J. Caro, Mater. Res. Bull. 98 (2018) 308–313.
[48] C.P. Bai, J.C. Bi, J.B. Wu, H. Meng, Y. Xu, Y.D. Han, X. Zhang, Appl. Organomet. Chem. 32 (2018) 7.
[49] S. Abdpour, E. Kowsari, M.R.A. Moghaddam, J. Solid State Chem. 262 (2018) 172–180.
[50] Y. Jiang, Z. Sun, C. Tang, Y. Zhou, L. Zeng, L. Huang, Appl. Catal. B 240 (2019) 30–38.
[51] W. Liu, M. Huang, C. Tang, B. Yin, Z. Gao, L. Li, J. Tang, L. Lei, X. Zhang Cui, Chem. Eng. J. 359 (2019) 254–264.
[52] S.K. Patra, S. Rahut, J.K. Basu, New J. Chem. 42 (2018) 18598–18607.
[53] H. Yi, D.L. Huang, L. Qin, G.M. Zeng, C. Lai, M. Cheng, S.J. Ye, B. Song, X.Y. Ren, X.Y. Guo, Appl. Catal. B-Environ. 239 (2018) 408–424.
[54] C. Zhou, C. Lai, C. Zhang, G. Zeng, D. Huang, M. Cheng, L. Hu, W. Xiong, M. Chen, J. Wang, Y. Yang, L. Jiang, Appl. Catal. B-Environ. 238 (2018) 6–18.
[55] M. Chen, G. Zeng, P. Xu, Y. Zhang, D. Jiang, S. Zhou, Environ. Sci. Nano 4 (2017) 720–727.
[56] F. Serre, C. Millange, M. Thouvenot, G. Nogues, D. Marsolier, G. Ferey Louer, J. Am. Chem. Soc. 124 (2002) 13519–13526.
[57] H. Yi, L. Qin, D.L. Huang, G.M. Zeng, C. Lai, X.G. Liu, B.S. Li, H. Wang, C.Y. Zhou, F.L. Huang, S.Y. Liu, X.Y. Guo, Chem. Eng. J. 358 (2019) 480–496.
[58] H. Tan, X. Gu, P. Kong, Z. Lian, B. Li, Z. Zheng, Appl. Catal. B-Environ. 242 (2019) 67–75.
[59] L.B. Jiang, X.Z. Yuan, G.M. Zeng, J. Liang, X.H. Chen, H.B. Yu, H. Wang, Z.B. Wu, J. Zhang, T. Xiong, Appl. Catal. B-Environ. 227 (2018) 376–385.
[60] Y. Yang, Z. Zeng, C. Zhang, D. Huang, G. Zeng, R. Xiao, C. Lai, C. Zhou, H. Guo, W. Xue, M. Cheng, W. Wang, J. Wang, Chem. Eng. J. 349 (2018) 808–821.
[61] B. Li, C. Lai, G. Zeng, L. Qin, H. Yi, D. Huang, C. Zhou, X. Liu, M. Cheng, P. Xu, C. Zhang, F. Huang, S. Liu, ACS Appl. Mater. Interfaces 10 (2018) 18824–18836.
[62] X. Hu, Y. Long, M. Fan, M. Yuan, H. Zhao, J. Ma, Z. Dong, Appl. Catal. B-Environ. 244 (2019) 25–35.
[63] R. Vakili, S.J. Xu, N. Al-Janabi, P. Gorgojo, S.M. Holmes, X.L. Fan, Microporous Mesoporous Mater. 260 (2018) 45–53.
[64] A.A. Oladipo, Process. Saf. Environ. Prot. 116 (2018) 413–423.
[65] M.-T.H. Nguyen, Q.-T. Nguyen, J. Photochem. Photobiol. A Chem. 288 (2014) 55–59.
[66] R. Liang, L. Shen, F. Jing, N. Qin, L. Wu, ACS Appl. Mater. Interfaces 7 (2015) 9507–9515.
[67] C.P. Bai, J.C. Bi, J.B. Wu, H. Meng, Y. Xu, Y.D. Han, X. Zhang, Appl. Organomet. Chem. 32 (2018) 7.
[68] R. Lin, S. Li, J. Wang, J. Xu, C. Xu, J. Wang, C. Li, Z. Li, Inorg. Chem. Front. 5 (2018) 3170–3177.
[69] Y. Gao, S. Li, Y. Li, L. Yao, H. Zhang, Appl. Catal. B 202 (2017) 165–174.
[70] C.Y. Zhou, C. Lai, C. Zhang, G.M. Zeng, D.L. Huang, M. Cheng, L. Hu, W.P. Xiong, M. Chen, J.J. Wang, Y. Yang, L.B. Jiang, Appl. Catal. B-Environ. 238 (2018) 6–18.
[71] W.J. Wang, P. Xu, M. Chen, G.M. Zeng, C. Zhang, C.Y. Zhou, Y. Yang, D.L. Huang, C. Lai, M. Cheng, L. Hu, W.P. Xiong, H. Guo, M. Zhou, ACS Sustain. Chem. Eng. 6 (2018) 15503–15516.
[72] W. Liang, L. Li, J. Hou, N.D. Shepherd, T.D. Bennett, D.M. D'Alessandro, V. Chen, Chem. Sci. 9 (2018) 3508–3516.
[73] S. Cui, G.Q. Shan, L.Y. Zhu, Appl. Catal. B-Environ. 219 (2017) 249–258.